Nuclear Inst. and Methods in Physics Research, A 1031 (2022) 166509

Contents lists available at ScienceDirect

Nuclear Inst. and Methods in Physics Research, A

journal homepage: www.elsevier.com/locate/nima

Transport tests of the St. Benedict first-stage extraction system

C. Davis [a], O. Bruce [a,b], D.P. Burdette [a], T. Florenzo [a], B. Liu [a], J. Long [a], P.D. O'Malley [a], M.A. Yeck [a], M. Brodeur [a,*]

[a] Department of Physics, University of Notre Dame, Notre Dame, IN 46556, USA
[b] Spelman College, Atlanta, GA 30314, USA

ARTICLE INFO

Keywords:
Beam thermalization
Radiofrequency carpets
Radioactive ion beams

ABSTRACT

The Superallowed Transition BEta NEutrino Decay Ion Coincidence Trap (St. Benedict) aims to conduct precision tests of the standard model by allowing for a determination of the Fermi to Gamow–Teller mixing ratio for many mirror transitions. St. Benedict will include a gas cell, a differentially-pumped extraction system, a radio-frequency (RF) cooler and buncher, and a Paul trap where the measurement will take place. The extraction system will include a first section housing a RF carpet at a pressure of around 3 mbar, followed by a second section housing a radio-frequency quadrupole (RFQ) ion guide at a pressure of 2×10^{-3} mbar. Transport efficiency of potassium ions using the RF carpet in static gas was determined to be above 90% using the ion surfing method after optimizing the potentials applied to various electrodes.

1. Introduction

The Standard Model (SM) describes fundamental building blocks and interactions in our Universe. The SM predicts that the Cabibbo–Kobayashi–Maskawa (CKM) matrix, which relates regular quark mass eigenstates to their eigenstates under the weak interaction, should be unitary. One precise method of testing the unitarity of the CKM matrix is comparing the sum of the magnitude square of the top row's matrix elements, $|V_{ud}|^2 + |V_{us}|^2 + |V_{ub}|^2$, to one. Currently, unitarity falls short at the 2σ-level [1], a situation that arises after the publication of several new and consistent transition-independent radiative correction calculation results [2–5]. As a result, V_{ud}, which is affected by those calculations, is currently under scrutiny. The precise determination of V_{ud} can be obtained from pion decay, neutron decay, mixed mirror decay, and superallowed pure Fermi decay [6]. While superallowed pure Fermi decays currently provide the most precise determination of V_{ud}, confirmation of these results from other types of decay can point to new physics or systematic effects. Mixed mirror decays do not present the same experimental challenges as pion and neutron decays, however V_{ud} can only be extracted precisely for five mixed mirror transitions due to a missing experimental quantity, the Fermi to Gamow–Teller mixing ratio ρ [6].

The Superallowed Transition BEta NEutrino Decay Ion Coincidence Trap (St. Benedict) [7,8] at the University of Notre Dame (UND) aims to determine ρ for many superallowed mixed transitions for the first time. St. Benedict will be located at UND's Nuclear Science Laboratory behind the TwinSol facility [9], which produces energetic radioactive ion beams (RIB) using transfer reactions. The components of St. Benedict include a large-volume gas catcher, a radio-frequency (RF) carpet, an ion guide, a radio-frequency quadrupole (RFQ) cooler and buncher [10], and a Paul trap [11]. Because the RIB are too energetic to be captured in a Paul trap, a gas catcher is required to thermalize the RIB using a helium buffer gas. In the gas catcher, the thermalized ions will be transported to an orifice using a combination of electrostatic and dynamic fields. Upon exiting the orifice, the ions will be accelerated towards a RF carpet that will transport them towards a second orifice (concentric with the first) leading to a chamber housing a RFQ ion guide. After, the ions will enter another RFQ which will cool and bunch the beam. Finally, the bunched beam will be delivered to a Paul trap where it will be confined using alternating and static electric fields. The Fermi-to-Gamow Teller mixing ratio will be determined from the $\beta - \nu$ angular correlation parameter, which will be fitted from the time the recoiling daughter nuclei take to reach a detector that will be placed away from the axis of the trap [11].

This paper reports on the differential pumping studies of the gas cell and the RF carpet vacuum chamber and the commissioning of the St. Benedict RF carpet at the planned operating pressure of ~3 mbar. As part of the commissioning, the potential on the various electrodes of the RF carpet and its setup were adjusted to optimize transport efficiency though the carpet central orifice and onto a collection disk.

2. Differential pumping

With an energy varying from 10–40 MeV, the RIB produced at TwinSol are too energetic to be captured in a Paul trap, and hence

* Corresponding author.
E-mail address: mbrodeur@nd.edu (M. Brodeur).

https://doi.org/10.1016/j.nima.2022.166509
Received 19 October 2021; Received in revised form 31 January 2022; Accepted 18 February 2022
Available online 4 March 2022

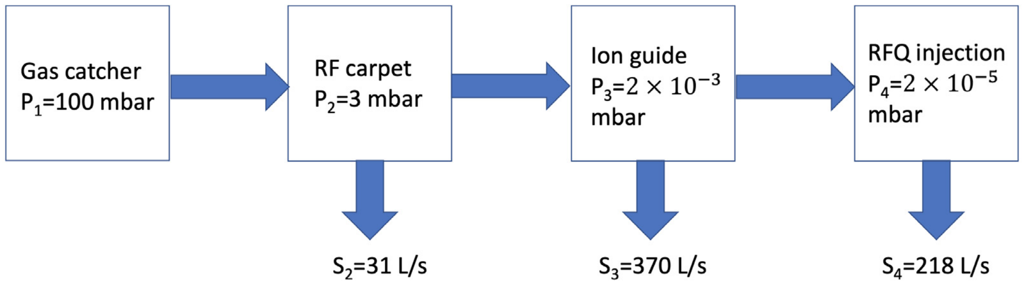

Fig. 1. The block diagram of the various differentially pumped chambers of St. Benedict, including the gas catcher, the RF carpet, the ion guide, and the RFQ injection chamber. Blue arrows between chambers represent gas flow through the connecting pipes, while the blue arrows exiting the chambers represent gas flow being pumped. The pressure of each chamber along with the pumping speeds of the pumps connected to the RF carpet, ion guide, and RFQ injection chambers are shown.

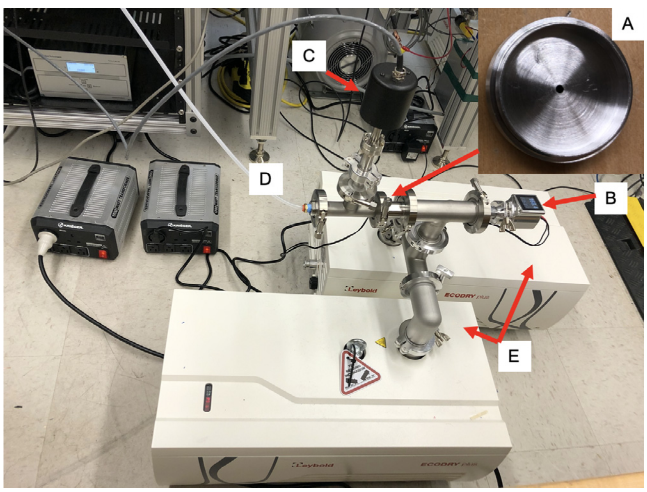

Fig. 2. Experimental setup for measuring pressures in two chambers connected by a narrow aperture (A), with two Ecodry 65 Plus pumps in parallel (E) connected to the second chamber. This image shows the MKS 121AA absolute pressure transducer (C) connected to the first chamber, where helium gas enters from the left (D). The pressure in the second chamber is measured using a MKS 902B absolute piezo vacuum pressure transducer (B).

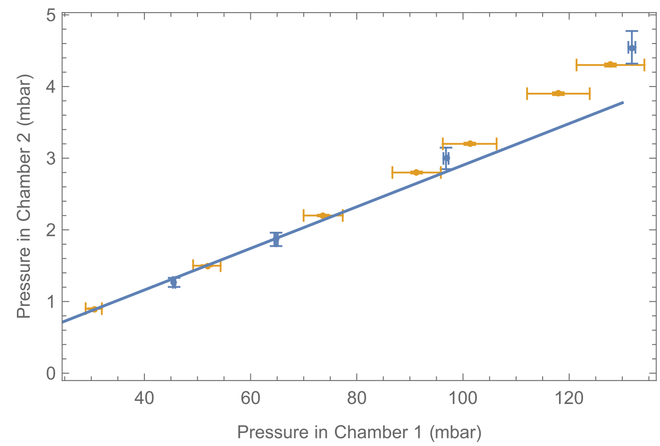

Fig. 3. Calculated pressures in the second chamber as a function of the pressure in the first chamber, for the pumping speed and aperture dimensions given in the text. The blue points represent experimental data with the MKS 121AA measuring pressure in the first chamber and the MKS 902B in the second, and the yellow points show results from the reverse configuration.

need to be stopped in a large volume gas catcher before forming a slow beam. For that purpose, a 830 mm-long gas catcher previously from Argonne National Laboratory will be used. The transport of that beam from the gas catcher requires the use of several differential pumping regions. As shown in Fig. 1, St. Benedict will have two chambers after the gas catcher and before the RFQ cooler and buncher: one housing a RF carpet at 3 mbar and the other housing an ion guide at 2×10^{-3} mbar (assuming the gas catcher is maintained at a pressure of 100 mbar). These pressures were predicted by solving a system of equations involving the pump throughput for each chamber and the flow through each pipe between chambers [12]. Choked viscous flow was used between the gas catcher, RF carpet and ion guide chambers. Molecular flow was used between the ion guide and RFQ injection chambers. The RF carpet chamber is pumped by two Leybold Ecodry 65 plus [13] (55 m^3/h each), the ion guide chamber will be pumped by two 250 L/s Agilent TwisTorr 300 turbomolecular pumps [14] (resulting in 370 L/s total after including reduction in pumping speed due to the inlet pressure and conductance losses) and the RFQ injection section will by pumped by one 360 L/s Leybold TurboVac [13] turbomolecular pump (reduced to 218 L/s after conductance losses).

The theoretical pressure calculations were tested experimentally using a test setup involving two Ecodry 65 plus pumps in parallel (Fig. 2). Pressures were measured in two connected chambers using a MKS 121AA absolute pressure transducer and a MKS 902B absolute piezo vacuum pressure transducer [15]. The chambers were connected by a narrow aperture with a hole diameter of 1.42 mm and a thickness of 0.576 mm. These dimensions will be similar to those of the aperture that will be used in St. Benedict.

As can be seen in Fig. 3, the experimental measurements matched the predictions well, especially for initial pressures of 100 mbar or lower. This measurement provided confidence in our pressure calculation, which was then used to estimate the pressure at which we should be testing the RF carpet. Assuming a typical gas catcher operating pressure of 100 mbar, we calculated, based on our pumping power and aperture size, that we will need a pressure of 3 mbar for our tests.

3. The St. Benedict RF carpet

The RF carpet, shown in Fig. 4, that will be used at St. Benedict to help guide the ions as they travel through the region of 3 mbar pressure, uses a design from the RIKEN SLOWRI group and has been manufactured by StaRflex Inc [16]. There are four different groups of electrodes (A, B, C, and D), which allows for the creation of a four-phase traveling wave. The first two electrodes (0 and 1) surrounding the orifice are connected separately, allowing the application of different signal from the rest of the carpet to facilitate the transmission through the orifice. However, for those tests, electrode 1 and B were connected together internally. Electrode 0, later referred to as the "hole" electrode, had a separate connection outside the chamber. The width of electrodes 1, A, B, C, and D are 0.0050(5)" (127 μm), while electrode 0 is 0.0030(5)" (76 μm) wide. The gaps between the electrodes are 0.0070(5)" (178 μm) and the orifice at the center of the carpet has a diameter of 0.0290(5)" (737 μm). The carpet is formed of 0.0012(1)" (30 μm)-thick nickel and gold plated copper on top of a 0.0018(1)" (52 μm)-thick flexible kapton

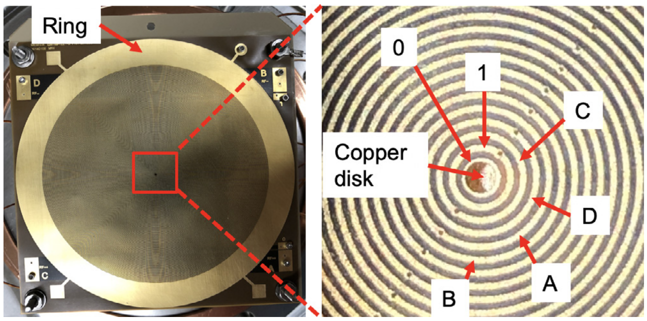

Fig. 4. The RF carpet used for the measurements (left). Visible are connections for electrodes A, B, C, and D as well as their locations from the center of the carpet (right). For these tests electrodes 1 and B were internally connected. Electrode 0, which connection was kept separate, will be referred to as the "hole" electrode. The outer ring electrode location is also indicated. The copper disk, located under the carpet, can also be seen.

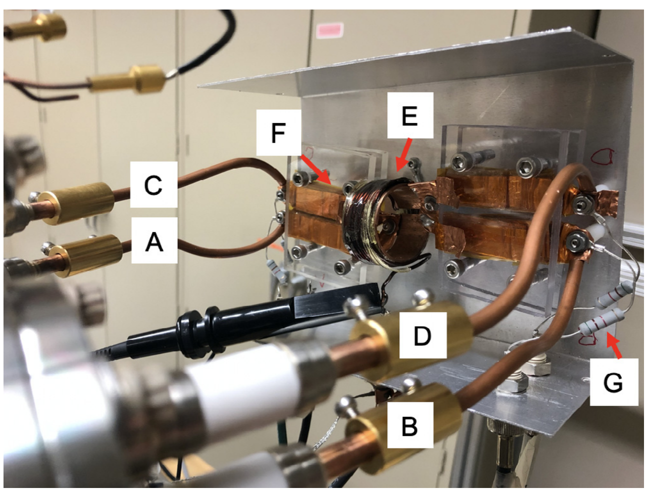

Fig. 5. RF carpet circuit attached to the chamber feedthrough. Components of the circuit include four copper tubes connecting to electrodes (A), (B), (C) and (D), air core impedance matching transformer (E), variable capacitors created using strips of copper insulated with Kapton tape and folded between two adjustable plastic plates (F) and 5.1k Ω resistors (G) that are part of the low-pass filter for the LF.

substrate. All reported values are from post-production measurement. Each strip of a given electrode is connected together on the back of the carpet through open vias. The carpet has a diameter of 8.10(5) cm and it is surrounded by the 0.90(5) cm wide "ring" electrode.

4. Transport method

To successfully transport the ions above the carpet, we need to repel the ions from the carpet and drag them towards the center. The repulsion is generated by potentials oscillating at RF and applied with a 180° phase shift between adjacent electrodes. Simultaneously, a so-called push force F_p, provided by applying a greater potential on a plate above the carpet, keeps the ions balanced (between that pushing force and the repulsion from the RF) above the carpet surface. Finally, the ions are dragged using the method of ion surfing [17–19], which involves overlaying a low frequency (LF) alternating signal to form an overall traveling wave.

The RF is produced by a T&C Power Conversion AG 1020 Generator [20]. An air-core transformer (see Fig. 5) was formed using a sliced copper tube of dimensions 32 mm in length and 34 mm in diameter for the secondary and surrounded by 9 turns of 14 AWG magnet wires for the primary. This transformer serves as impedance matching and creates the 0° and 180° phases. To minimize resistive losses, copper

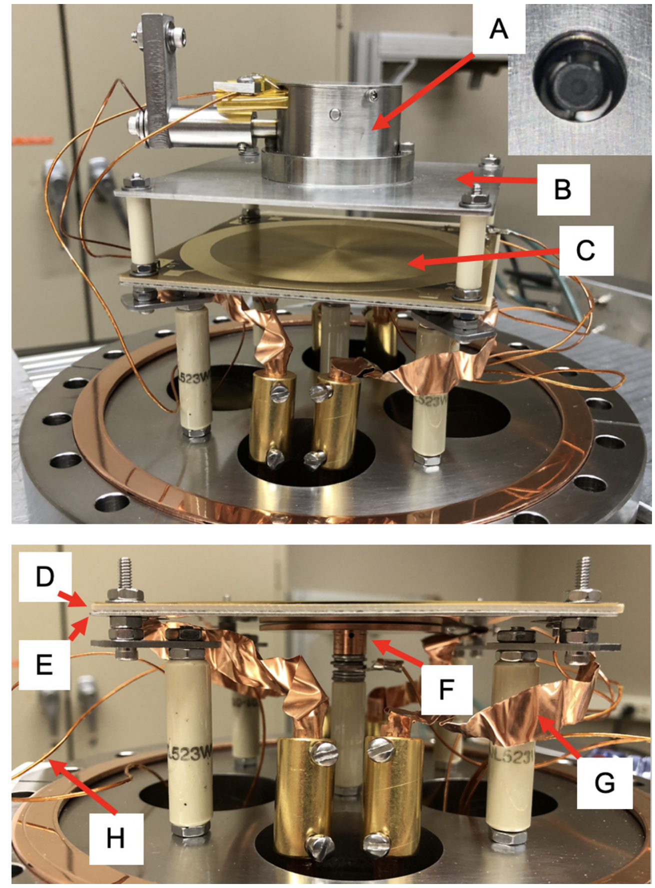

Fig. 6. RF carpet on its support frame. Important components include (A) the ion source in its assembly, (B) the plate creating the electric field that pushes the ions towards the carpet, (C) the RF carpet (located 2.3 cm below the plate), (D) a sheet of PEEK insulating the RF carpet and the stainless steel plate with the 1/16" aperture, (E) a stainless steel sheet with the 1/16" aperture, (F) a copper disk collecting the transported ions, (G) copper strips carrying the RF and LF, and (H) Kapton-coated DC connections.

was used as material to transport the RF whenever possible, and we also minimized the number of connections. These connections were also made as short as possible (while having a large surface area) to not only reduce resistive losses, but also the overall inductance of the circuit. For this reason, 3/16" (4.8 mm) outer diameter copper tubes were used to connect the RF circuit to the 1/4" (6.4 mm) diameter copper feedthrough via beryllium copper connectors (Fig. 5, 7). Under vacuum, 1/2" (12.7 mm) wide copper strips were used to connect the signal to the carpet (Fig. 6).

The LF is produced by a Rigol DG1000Z [21] two-channel arbitrary waveform generator. The two channel outputs are phase shifted by 90° and then these two signals are fed to AD817 operational amplifiers [22] to introduce a 180° phase shift on them, creating the four phases needed to produce the traveling wave.

It should be noted that for these measurements no RF nor LF signals were applied on the hole electrode, which was maintained at a fixed, but variable potential (see Section 8.4). This choice was guided by simulations using the ion optical package SIMION that revealed an optimal transport efficiency through the orifice when no RF nor LF signals are present.

5. RF carpet test setup

The RF carpet support frame (Fig. 6) includes a potassium thermionic source model 101139-03 [23] centered on top of a stainless

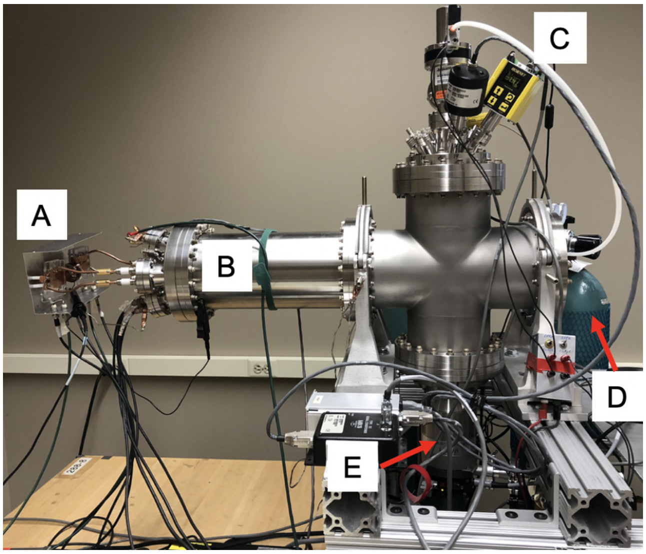

Fig. 7. Experimental setup used for testing the RF carpet. (A) RF circuit connected to the flange on which the RF carpet and ion source are attached. (B) Location of the RF carpet in the vacuum chamber. (C) Various vacuum gauges used for the measurements. (D) Ultra-high purity (99.999% pure) helium bottle. (E) Turbo molecular pump.

Fig. 8. Experimental setup used to investigate the content of the thermionic ion source. (A) Residual gas analyzer. (B) Location of the ion source in the middle of a 6" ConFlat cross. (C) Ion source (turned ON) and pointing away from the RGA. (D) Ion source pointing towards the RGA. (E) Viewport used to observe the ion source.

steel plate with a 12 mm diameter aperture in the center. Such source was chosen based on its ease to produce an ion beam with a high purity (see next section) and because alkali ions undergo a minimal amount of charge exchange reaction (potential loss mechanism) with other species. The radioactive isotopes planned to be transported by the RF carpet at St. Benedict will range from ^{11}C to ^{41}Sc. Hence, ^{39,41}K falls on the high-end of that mass range. The lighter ^{23}Na was not chosen for the studies since based on past experience, it typically contains potassium contamination that can skew the results. Note that some of the planned radioactive isotopes could be transported in molecular form to increase their mass and transport efficiency.

A larger potential is applied to the stainless steel plate as compared to the carpet in order to drag ions towards the carpet, where they would be transported towards its central orifice using DC potentials, as well as RF and LF signals. Below the carpet, a 1/16" (1.6 mm) thick sheet of PEEK with a 1/8" (3.2 mm) hole insulates the RF carpet from a 0.030" (0.76 mm) thick stainless steel plate that has a 1/16" (1.6 mm) diameter aperture (indicated by "E" in Fig. 6) where the ions are transported through until they are collected on a copper disk. The potential applied on the aperture as well as the other electrodes is given in Table 1. Because we are interested in testing the transport of ions close to the actual configuration that will be employed at St. Benedict, the ion source was installed some distance directly above the RF carpet orifice.

The RF carpet is placed in a vacuum chamber that includes (Fig. 7) an InstruTech IGM402 Hornet Ionization gauge and a convection gauge [24] used for low-pressure reading in the absence of helium. A MKS Baratron Type 121AA absolute pressure transducer [15] was used to accurately measure the helium pressure during our measurements. The chamber was evacuated between each measurements using a Leybold TurboVac 90 L/s turbo molecular pump backed by an Ecodry 65 plus [13]. Ultra high purity (99.999% pure) helium has been used for the measurements and a Keithley 6514 Electrometer [25] was used to measure the various currents.

6. Isotopes produced by the ion source

The purity of the potassium beam produced by the thermionic source was investigated using a SRS RGA200 residual gas analyzer (RGA) [26] prior to the RF carpet transport studies. The setup is shown on Fig. 8 and consisted of a thermionic ion source attached to a rotational actuator that allowed it to be pointed either towards the RGA or away from it. The chamber was evacuated with the same pumping system and contained the same gauges as for the RF carpet transport studies. The ion source was operated at a base pressure of $1.2{\times}10^{-8}$ mbar. For the measurements the RGA ionizer was turned off and the ion beam produced was shot directly at it.

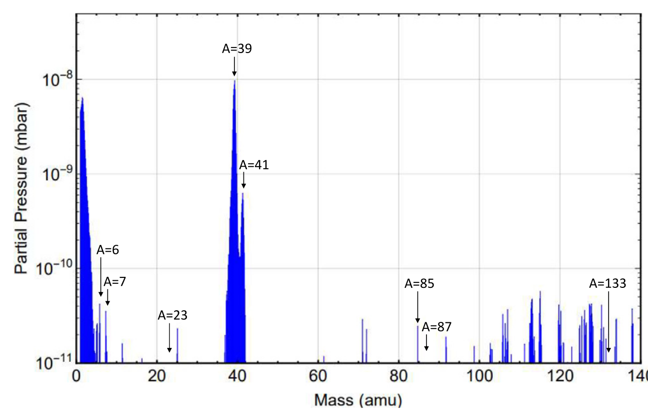

Fig. 9. RGA partial pressure scan with the ion beam from the potassium thermionic source directed towards it. A = 39 and 41, corresponding to ^{39}K$^+$ and ^{41}K$^+$, are clearly present with their natural abundance. The location of other possible alkali contaminants (^{6,7}K$^+$, ^{23}Na$^+$, ^{85,87}Rb$^+$, and ^{133}Cs$^+$) not seen is also indicated. The large peak at $A < 2$ is from ions sufficiently energetic to pass through the quadrupole mass filter when the applied potentials are low.

Fig. 9 shows the average of ten RGA partial pressure scans with the ion source directed towards it. The two stable isotopes of potassium ^{39}K (93.3% natural abundance) and ^{41}K (6.7% natural abundance) are clearly dominant species. No conclusive evidence of other possible alkali contaminants (^{6,7}Li$^+$, ^{23}Na$^+$, ^{85,87}Rb$^+$, and ^{133}Cs$^+$) can be seen. The large peak at low mass ($A < 2$) is an artifact coming from ions sufficiently energetic to pass through the quadrupole mass filter when the applied potentials are low. For the measurements presented in Fig. 9 a current of 1.60 A corresponding to a potential difference of 4.1 V, was applied across the ion source filament. Potentials of 40 V and 30 V were

Table 1
Potentials on various electrodes leading to a transport efficiency above 90% at 3.5 mbar. See text for more details and Figs. 6 and 4, to see the location of each electrode.

Electrode	Potential (V)
Source	172.5
Plate	150.0
Carpet	100.0
Ring	110.0
Hole	48.5
Aperture	10
Disk	0

also applied to the ion source and the anode facing it to accelerate the ion beam towards the RGA.

7. Measurement method

The main calculated quantity in this investigation was the transport efficiency, which is defined as the ratio of the electric current produced by the transported ions to the collection disk over the ion beam current from the ion source that passed the push field plate and head towards the center of the carpet. That latter current was taken as the sum of the current hitting the carpet in the absence of RF and LF, the hole electrode and the collection plate. It should be noted that at a few mbar of pressure the thermal ions will follow the field lines and hit various electrode. They will not collect on the Kapton between the electrodes.

To minimize residual air contamination in the chamber, the chamber was evacuated with a turbo pump between measurements down to less than 1×10^{-8} mbar. Before each measurement, the chamber was flushed once with 20 mbar of helium. After injecting the desired amount of helium, we heated the ion source by running a current (e.g. ≈2.45 A at 3.2 mbar) through its filament. The ion beam current took approximately an hour to stabilize after which we started our measurements. For each measurement, the ion source potential was adjusted to get a current on the carpet of around 100 pA.

For a typical measurement, the voltages applied to the carpet, hole electrode, push plate, or aperture were adjusted and RF and LF were applied to the carpet to transport the ions.

8. Ion transport to the collection disk

The ion transport efficiency to the collection disk has been measured for a helium pressure ranging from 3.2 to 3.5 mbar from one measurement to another. The potentials on the various electrodes were adjusted to maximize the transport efficiency. Results from simulations performed with the ion optical package SIMION served as starting point for the optimization process in the laboratory.

A traveling wave frequency of 50 kHz, which for a 4-phases wave on a 0.32 mm pitch carpet corresponds to a traveling wave speed of 64 m/s, and a zero-to-peak amplitude of 3 V were chosen for all the presented results since it resulted in efficient transport based on simulations and initial tuning. The RF carpet was driven on-resonance at 12.26 MHz. Unless otherwise noted, a zero-to-peak RF amplitude of 75 V, just below the RF discharge limit, has been used.

Table 1 gives the various potentials that led to a transport efficiency above 90% at 3.2 mbar. These will be the "default" potentials in this section unless otherwise noted.

The disk electrode where the ions were collected was grounded to facilitate a precise reading of the transported ion beam currents. A difference of potential of only 10 V between the aperture and the disk electrode was found to be sufficient to prevent beam loss on the aperture.

For the various measurements, the potential of the ion source was adjusted to produce an ion beam current of 100 pA. Typically, the potential difference between the ion source and the plate was around 22.5 V. While higher efficiencies are seen for lower potential differences, the lower current results in a less precise determination of the efficiency.

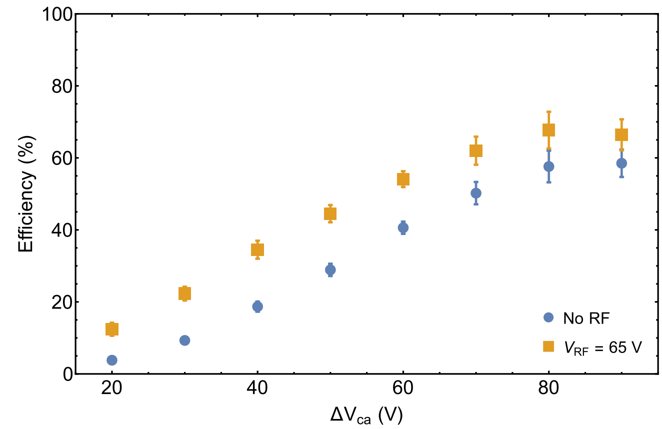

Fig. 10. Transport efficiency to the collection disk as function of the carpet–aperture potential difference ΔV_{ca}, without the application of RF nor LF as well as with the application of LF and 65 V zero-to-peak RF amplitude. See text for more details.

8.1. Effect of the carpet–aperture potential difference

Fig. 10 shows the transport efficiency to the collection disk as a function of the carpet–aperture potential difference ΔV_{ca}. For that measurement the potential of the hole electrode relative to the carpet and the aperture was held fixed at $(V_{carpet} - V_{hole})/(V_{carpet} - V_{aperture}) = 1/3$, the plate-to-carpet potential difference was held fixed at 70 V, and the aperture was held at 30 V. All of these values were found to lead to an efficient transport in previous scans. The efficiency is found to gradually increase with ΔV_{ca} until it plateaus for $\Delta V_{ca} > 80$ V. We did not go to higher potentials due to discharge limitations. Fig. 10 shows that the transport efficiency with a 65 V RF amplitude follows a similar behavior as the one without RF and LF, while being about 15% higher. This indicates that the potential configuration from the carpet to the collection disk strongly affects the transport of the ions. It should be noted that by keeping the potential of the hole electrode relative to the carpet and aperture fixed, the source-to-hole potential difference changes by 24 V over the 70 V variation in ΔV_{ca} studied. This will also have an effect on the transported current to the collection disk. Hence, in the next section we studied the effect of the ion source potential on the transport efficiency.

8.2. Effect of the source-to-plate potential difference

The potential difference between the ion source and the plate ΔV_{sp} will affect the intensity of the beam extracted from the source, the strength of the "pushing force" near the carpet orifice, as well as the focusing of this ion beam towards the RF carpet orifice. The effect of ΔV_{sp} on the transport efficiency was studied for a 75 V zero-to-peak RF amplitude, 50 kHz, 3 V amplitude traveling wave at a pressure of 3.5 mbar. The plate had a potential of 120 V, the carpet and hole electrode were both biased at 60 V, and the aperture was grounded. Fig. 11 shows that increasing ΔV_{sp} results in a small decrease in the transport efficiency. This could be attributed to a stronger "pushing force" near the carpet orifice or a widening of the beam spot at the carpet location (and less focused towards the orifice), an effect seen in simulations. Another possibility would be that it is due to the increased space charge passing through the orifice as the ion beam current increase from 10 to 260 pA. The effect of high ion beam current on transport through an orifice has been studied extensively for the Advanced Cryogenic Gas Stopper (ACGS) [27]. These experimental studies were done for a slightly larger orifice of 1 mm diameter and at a room temperature pressure of 50 Torr. They showed about 100% transport efficiencies up to around 1 nA beam current, followed by a decline in the 1–10 nA current range. This is well above the beam current used in our studies.

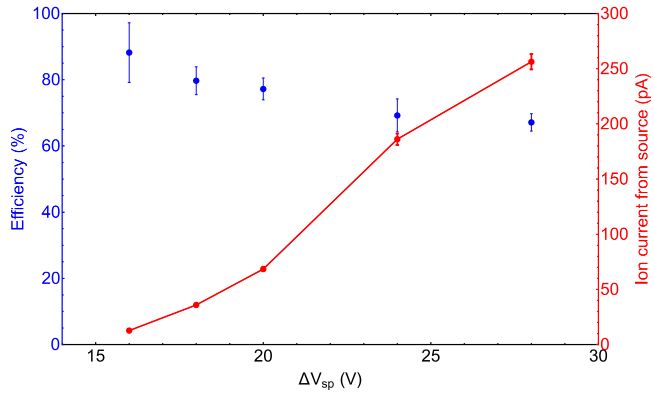

Fig. 11. Transport efficiency to the collection disk (unconnected circles) and ion current from the source heading towards the carpet (connected circles) as function of the source-to-plate potential difference ΔV_{sp} with the application of LF and 75 V zero-to-peak RF amplitude. See text for more details.

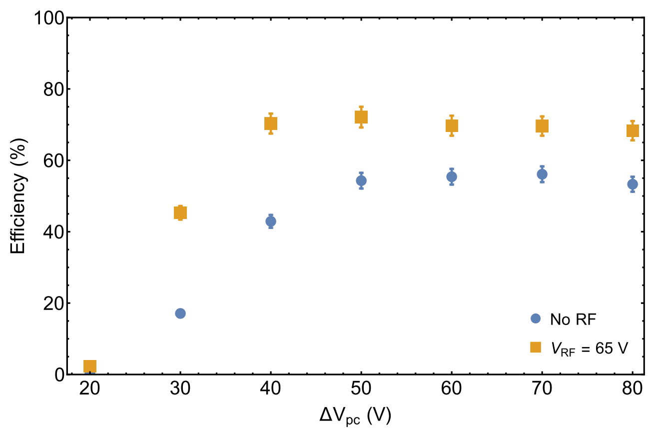

Fig. 12. Transport efficiency to the collection disk as function of the plate-to-carpet potential difference ΔV_{pc}, without the application of RF nor LF as well as with the application of LF and 65 V zero-to-peak RF amplitude. Transport efficiency for ΔV_{pc} = 20 V without RF and LF is consistent with zero. See text for more details.

Furthermore, their particle-in-cell simulations done in the pressure range of 10–30 Torr at 50 K indicates a tapering in the efficiency drop due to increased beam current when the pressure is lower. Hence, in conclusion, the weakening of the transport efficiency with ΔV_{sp} is most likely not due to the change in beam current but rather the ion optics focusing the beam towards the orifice.

8.3. Effect of the plate-to-carpet potential difference

Next, the plate-to-carpet potential difference ΔV_{pc} was varied and the results are presented in Fig. 12. For that measurement the hole electrode potential was 65 V. Even with the absence of the RF and LF signals, transport efficiencies above 50% are achieved if ΔV_{pc} is at least 50 V. Once again, this indicates that the potential configuration from the ion source to the collection disk can greatly help in having an efficient transport. The application of a 65 V RF and a 50 kHz, 3 V amplitude traveling wave increases the transport efficiency to above 70%. At the same time, the application of these signals extends the plateau region where an efficient transport is observed.

8.4. Effect of the carpet–hole potential difference

Finally, using the previously found optimal potentials, we varied the potential on the hole electrode. The results for RF amplitudes of 65 V and 75 V as well as no RF are shown in Fig. 13. The rapid drop in

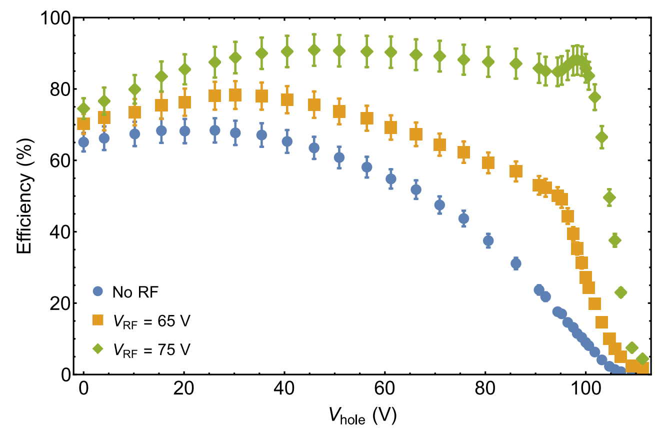

Fig. 13. Transport efficiency to the collection disk as function of the hole electrode potential V_{hole} without the application of RF nor LF as well as with the application of LF and 65 V or 75 V zero-to-peak RF amplitude. See text for more details.

efficiency for V_{hole} > 100 V is due to the potential of this electrode exceeding the potential of the RF carpet making the jump in the hole more difficult. Once again the efficiency with RF and LF closely follow the behavior of the efficiency without these signals, especially for the lower values of V_{hole} where the large carpet–hole electrode potential difference helps guide the ions into the hole. The application of the RF and LF mostly affects the transport efficiency at larger values of V_{hole}. Fig. 13 also shows that a 10 V increase in RF amplitude from 65 V to 75 V (just below the discharge limit) brings the optimal efficiency from just below 80% to above 90%.

9. Conclusion

The St. Benedict ion trapping system, currently under construction at the University of Notre Dame NSL aims to test the Standard Model using nuclear beta decay between isobaric analogue states of mirror nuclei. The instrument will comprise a large volume gas catcher, a differentially-pumped extraction system, a radio-frequency quadrupole cooler and buncher, as well as a Paul trap were the measurement will take place. We first reported differential pumping tests of the extraction system. Second, the transport efficiency of the first stage of the St. Benedict extraction system, which includes an RF carpet, was determined to be above 90% using potassium ions in static gas after optimizing the pushing RF and LF traveling waves and the potentials applied to the ion source, push plate, RF carpet, ring electrode, hole electrode, aperture, and collection disk at a pressure of 3.5 mbar. Similar transport efficiency should be expected from other species since most of the transport is accomplished by electrostatic fields and the RF carpet only provide an additional 25% efficiency in the transport. Furthermore, because most of the transport is electrostatic, the orifice of the gas catcher will have to be precisely aligned with the RF carpet one. The next RF carpet testing phase will consist of testing the extraction of ions in the differential pumping system planned to be used for St. Benedict with the presence of gas flow and the gas jet from the gas catcher. Once assembled, St. Benedict will conduct precision test of the standard model by allowing for a determination of V_{ud} for the lightest mirror transitions.

CRediT authorship contribution statement

C. Davis: Software, Formal analysis, Investigation, Writing – original draft. **O. Bruce:** Software, Formal analysis, Investigation. **D.P. Burdette:** Investigation. **T. Florenzo:** Investigation. **B. Liu:** Investigation, Writing – review & editing. **J. Long:** Investigation. **P.D. O'Malley:**

Investigation. **M.A. Yeck:** Software, Formal analysis, Investigation. **M. Brodeur:** Conceptualization, Methodology, Software, Formal analysis, Investigation, Writing – review & editing, Supervision, Project administration, Funding acquisition.

Declaration of competing interest

The authors declare that they have no known competing financial interests or personal relationships that could have appeared to influence the work reported in this paper.

Acknowledgments

We would like to thank P. Schury and M. Wada for providing the design file of the RF carpet used in this study. This work was conducted with the support of the National Science Foundation, USA under Grant PHY-1725711, PHY-2011890, PHY-2050527, and of the University of Notre Dame, USA.

References

[1] J.C. Hardy, I.S. Towner, Superallowed $0^+ \rightarrow 0^+$ nuclear β decays: 2020 critical survey, with implications for V_{ud} and CKM unitarity, Phys. Rev. C 102 (2020) 045501, http://dx.doi.org/10.1103/PhysRevC.102.045501, https://link.aps.org/doi/10.1103/PhysRevC.102.045501.

[2] C.-Y. Seng, M. Gorchtein, H.H. Patel, M.J. Ramsey-Musolf, Reduced hadronic uncertainty in the determination of V_{ud}, Phys. Rev. Lett. 121 (2018) 241804, https://link.aps.org/doi/10.1103/PhysRevLett.121.241804.

[3] C.-Y. Seng, X. Feng, M. Gorchtein, L.-C. Jin, Joint lattice QCD–dispersion theory analysis confirms the quark-mixing top-row unitarity deficit, Phys. Rev. D 101 (2020) 111301, http://dx.doi.org/10.1103/PhysRevD.101.111301, https://link.aps.org/doi/10.1103/PhysRevD.101.111301.

[4] A. Czarnecki, W.J. Marciano, A. Sirlin, Radiative corrections to neutron and nuclear beta decays revisited, Phys. Rev. D 100 (2019) 073008, http://dx.doi.org/10.1103/PhysRevD.100.073008, https://link.aps.org/doi/10.1103/PhysRevD.100.073008.

[5] L. Hayen, Radiative corrections to nucleon weak charges and beyond standard model impact, 2021, arXiv:2102.03458.

[6] O. Naviliat-Cuncic, N. Severijns, Phys. Rev. Lett. 102 (2009) 142302, http://link.aps.org/doi/10.1103/PhysRevLett.102.142302.

[7] M. Brodeur, J. Kelly, J. Long, C. Nicoloff, B. Schultz, $[V]_{ud}$ determination from light nuclide mirror transitions, Nucl. Instrum. Methods Phys. Res. B 376 (2016) 281–283, http://dx.doi.org/10.1016/j.nimb.2015.12.038, Proceedings of the {XVIIth} International Conference on Electromagnetic Isotope Separators and Related Topics (EMIS2015), Grand Rapids, MI, U.S.A., 11-15 2015, http://www.sciencedirect.com/science/article/pii/S0168583X15012847.

[8] P. O'Malley, M. Brodeur, D. Burdette, J. Klimes, A. Valverde, J. Clark, G. Savard, R. Ringle, V. Varentsov, Testing the weak interaction using st, benedict at the university of notre dame, Nucl. Instrum. Methods Phys. Res. Sec. B 463 (2020) 488–490, https://www.sciencedirect.com/science/article/pii/S0168583X19302010.

[9] F. Becchetti, M. Lee, T. O'Donnell, D. Roberts, J. Kolata, L. Lamm, G. Rogachev, V. Guimarẽs, P. DeYoung, S. Vincent, The TwinSol low-energy radioactive nuclear beam apparatus: status and recent results, Nucl. Instrum. Methods Phys. Res. A 505 (2003) 377–380, http://dx.doi.org/10.1016/S0168-9002(03)01101-X, proceedings of the tenth Symposium on Radiation Measurements and Applications, http://www.sciencedirect.com/science/article/pii/S016890020301101X.

[10] A.A. Valverde, M. Brodeur, D.P. Burdette, J.A. Clark, J.W. Klimes, D. Lascar, P.D. O'Malley, R. Ringle, G. Savard, V. Varentsov, Stopped bunched beams for the TwinSol facility, Hyperfine Interact 240 (1) (2019) 38, http://dx.doi.org/10.1007/s10751-019-1591-x.

[11] D. Burdette, M. Brodeur, P. O'Malley, A. Valverde, Development of the st, benedict paul trap at the nuclear science laboratory, Hyperfine Interact. 240 (1) (2019) 70, http://dx.doi.org/10.1007/s10751-019-1606-7.

[12] K. Jousten, Handbook of Vacuum Technology, Wiley-VCH, Weinheim, Germany, 2016.

[13] Leybold, https://www.leybold.com/us/en/.

[14] Agilent, https://www.agilent.com/.

[15] MKS, https://www.mksinst.com/.

[16] Starflex inc, http://www.starflex.com/.

[17] G. Bollen, Ion surfing with radiofrequency carpets, Int. J. Mass Spectrom. 299 (2) (2011) 131–138, http://dx.doi.org/10.1016/j.ijms.2010.09.032, https://www.sciencedirect.com/science/article/pii/S1387380610003659.

[18] M. Brodeur, A. Gehring, G. Bollen, S. Schwarz, D. Morrissey, Experimental investigation of the ion surfing transport method, Int. J. Mass Spectrom. 336 (2013) 53–60, https://www.sciencedirect.com/science/article/pii/S138738061200437X.

[19] F. Arai, Y. Ito, M. Wada, P. Schury, T. Sonoda, H. Mita, Investigation of the ion surfing transport method with a circular RF carpet, Int. J. Mass Spectrom. 362 (2014) 56–58, https://www.sciencedirect.com/science/article/pii/S1387380614000098.

[20] T & C power conversion, https://www.tcpowerconversion.com/.

[21] Rigol, https://www.rigolna.com/.

[22] Analog Device AD817, https://www.analog.com/media/en/technical-documentation/data-sheets/AD817.pdf.

[23] Heatwave labs, https://www.cathode.com/.

[24] Instrutech, https://www.instrutechinc.com/.

[25] Keithley, https://www.tek.com/keithley.

[26] RGA, https://www.thinksrs.com/products/rga.html.

[27] R. Ringle, G. Bollen, K. Lund, C. Nicoloff, S. Schwarz, C.S. Sumithrarachchi, A.C.C. Villari, Particle-in-cell techniques for the study of space charge effects in the advanced cryogenic gas stopper, Nucl. Instrum. Methods Phys. Res. Sec. B 496 (2021) 61–70, http://dx.doi.org/10.1016/j.nimb.2021.03.020, https://www.sciencedirect.com/science/article/pii/S0168583X21001117.